Micro and Nano Engineering 2 (2019) 117–121

Contents lists available at ScienceDirect

Micro and Nano Engineering

journal homepage: www.elsevier.com/locate/tsf

In-doped Sb nanowires grown by MOCVD for high speed phase change memories

R. Cecchini [a], S. Selmo [a,b], C. Wiemer [a], M. Fanciulli [a,b], E. Rotunno [c,1], L. Lazzarini [c], M. Rigato [d], D. Pogany [d], A. Lugstein [d], M. Longo [a,*]

[a] CNR-IMM, via C. Olivetti 2, 20864 Agrate Brianza, (MB), Italy
[b] Dipartimento di Scienza dei Materiali, University of Milano Bicocca, Via R. Cozzi 53, 20126 Milano, Italy
[c] CNR-IMEM, Parco Area delle Scienze 37/A, I-43124 Parma, Italy
[d] Institute for Solid State Electronics, TU Wien, Floragasse 7, A-1040 Vienna, Austria

ARTICLE INFO

Article history:
Received 28 June 2018
Received in revised form 12 September 2018
Accepted 7 November 2018

Keywords:
Phase change memories
Nanowires
MOCVD
In-Sb
TEM
XRD

ABSTRACT

We investigated the Phase Change Memory (PCM) capabilities of In-doped Sb nanowires (NWs) with diameters of (20–40) nm, which were self-assembled by Metalorganic Chemical Vapor Deposition (MOCVD) via the vapor-liquid-solid (VLS) mechanism. The PCM behavior of the NWs was proved, and it was shown to have relatively low reset power consumption (~ 400 μW) and fast switching capabilities with respect to standard Ge-Sb-Te based devices. In particular, reversible set and reset switches by voltage pulses as short as 25 ns were demonstrated. The obtained results are useful for understanding the effects of downscaling in PCM devices and for the exploration of innovative PCM architectures and materials.

1. Introduction

Phase Change Memory (PCM) technology is thought to be one of the most suitable candidates for the realization of the next generation high-density and high-performance non-volatile memory products [1], including those based on the recently proposed cross point architecture [2,3]. The crystallization speed, which closely relates to the device operation rate, plays a central role in the search for new PCM materials [4]. While the reference alloy for PCM is still $Ge_2Sb_2Te_5$, which belongs to the class of nucleation-dominated crystallization materials, other alloys with growth-dominated crystallization mechanism are being considered as fast-switching materials. Sb-based and Te-free phase-change materials, such as Ga–Sb, Ge–Sb and In–Sb, have been so far investigated primarily for optical devices (i.e. rewritable CDs), and have shown high crystallization speed and adequate amorphous phase stability [5–9]. The speed and thermal stability of In–Sb and doped In–Sb alloys have also been investigated in solid state thin film-based PCM devices [10,11]. However, the properties of In–Sb alloys in nanoscaled devices have not been studied, yet.

In the case of the PCM technology, downscaling can provide, in addition to higher storage density, a reduction of operation currents and power consumption. In this context, PCM nanowires (NWs) represent one of the ultimate examples of downscaling, featuring diameters down to few tens of nanometers and very high aspect ratios [12]. Both the reduction of the active volume and the self-heating mechanism are expected to produce a reduction of the switching currents and powers [13]. Such improvements have indeed been observed for NWs of $Ge_2Sb_2Te_5$ [14], GeTe [15], Sb_2Te_3 [16] and $In_3Sb_1Te_2$ alloys [17]. We previously reported on the growth of NWs of the ternary In-Sb-Te system by Metalorganic Chemical Vapor Deposition (MOCVD), coupled to the Vapor-Liquid-Solid mechanism (VLS) [18], which were used to make NWs-based PCM devices by the aid of an Electron Beam Lithography (EBL) process [19].

In this work, we used the same process to fabricate In-doped Sb NWs-based PCM devices. We then investigated them in terms of their PCM functionality and verified their low power and fast switching capabilities, both for set (low resistance state) and reset (high resistance state) operations.

2. Experimental

The self-assembly of the NWs was performed with an Aixtron AIX 200/4 MOCVD reactor, exploiting the VLS mechanism induced by Au

* Corresponding author at: CNR-IMM, via C. Olivetti 2, Agrate Brianza, Italy.
E-mail address: massimo.longo@mdm.imm.cnr.it (M. Longo).
[1] Current address: CNR-IMM, Zona industriale, Strada VIII n.5, 95121 Catania, Italy

https://doi.org/10.1016/j.mne.2018.11.002

metal-catalyst nanoparticles (NPs). The Au NPs were dispersed from a colloidal solution by British Bio Cell Company ® on single-crystal Si (111) and Si (100), (1×1) cm^2 substrates, after removal of the Si native oxide by immersion in a HF 5% solution. In Ref. [18], we described how NWs with different In-Sb-Te compositions, (namely $In_3Sb_1Te_2$ and In-doped Sb_4Te_1), and different morphologies, (namely tapered and non-tapered), could be obtained by varying the MOCVD process parameters, for a fixed Au NPs size of 10 nm. Here the same precursors, dimethyl aminopropyl-dimethyl-indium ($C_7H_{18}InN$), antimony-trichloride ($SbCl_3$) and bis-trimethylsilyl-telluride ($Te(SiMe_3)_2$), provided by Air Liquide ® (transported to the MOCVD reactor by an ultra-purified N_2 carrier/process gas [20]), were used on substrates prepared with 20 nm Au NPs, leading to the growth of thin and slightly tapered NWs, with an In-doped Sb shaft and a Te-rich base. In particular, the precursors partial pressures in the vapor phase were 1.2×10^{-3}, 7.4×10^{-3} and 2.9×10^{-2} mbar for $C_7H_{18}InN$, $SbCl_3$ and $Te(SiMe_3)_2$, respectively; the total gas flow was 4.5 L/min. The MOCVD reactor temperature and pressure were 325 °C and 300 mbar, respectively, while the growth time was 180 min.

The morphology, microstructure and composition of the NWs were characterized by Scanning Electron Microscopy (SEM), X-Ray Diffraction (XRD), High Resolution Transmission Electron Microscopy (HRTEM) and Energy Dispersive X-Ray (EDX) microanalysis. For the electrical characterization, the NWs were transferred onto insulating substrates and the two-terminal devices fabrication was completed by Electron Beam Lithography (EBL), evaporation of a Ni (20 nm)/Au (100 nm) stack and lift-off. The electrical measurements were performed by the Transmission Line Pulse (TLP) technique using a HPPI® system [21]. In particular, the electrical measurement set-up consisted of a 50 Ω high voltage pulse generator, a high speed digital oscilloscope and a Source Meter Unit (SMU). The pulse amplitudes and durations of the set and reset operations were assessed by direct measurement at the fabricated devices by the four-point Kelvin method. The read operation of the device state was performed by direct current (d.c.) measurements at 0.02 V after each pulse, using the switch configuration with the SMU.

3. Results and discussion

Fig. 1(a) shows an SEM image of the NWs grown on the Si (111) substrate. They have lengths in the range of (2-4) μm and diameters in the range of (20-40) nm, apart from a thicker base. Large area XRD on one of such as-grown samples is presented in Fig. 1(b). The data were simulated by Rietveld refinement by using the Sb rhombohedral structure and randomly oriented diffracting grains (Supplementary Information S1). The simulation of the diffracting maxima at low angle allowed us to extract the lattice parameters of the NWs. The obtained values are $a = 4.40$ Å and $c = 11.19$ Å, which correspond to a slightly higher cell volume than the one reported in the database (see Supplementary Information S1). Moreover, the different intensity of the low angle diffracting maxima, as compared to the powder pattern (red line in Fig. 1(b)) suggests that the NWs exhibit a preferential orientation.

The microstructure and composition of single NWs were measured by HRTEM and EDX. The EDX analysis (Supplementary Information S2), showed that Te is confined within the thick base portion of the NWs, while the NWs shaft is made of Sb and In, with a concentration of In that varies from 5 at. % near the NWs bottom, up to 15 at. % near the top. The atomic arrangement of one NW shaft is visible in the HRTEM images of Fig. 1(c) and (d). The corresponding FFT pattern, reported in Fig. 1(e), is consistent with the [001] projection of the rhombohedral structure of metallic Sb [22]. Consistently with the XRD analysis, the HRTEM measured cell parameter ($a = 4.4$ Å) is slightly larger than the one reported in the literature for metallic Sb ($a = 4.31$ Å). As indicated by the EDX measurements, this is most likely due to the

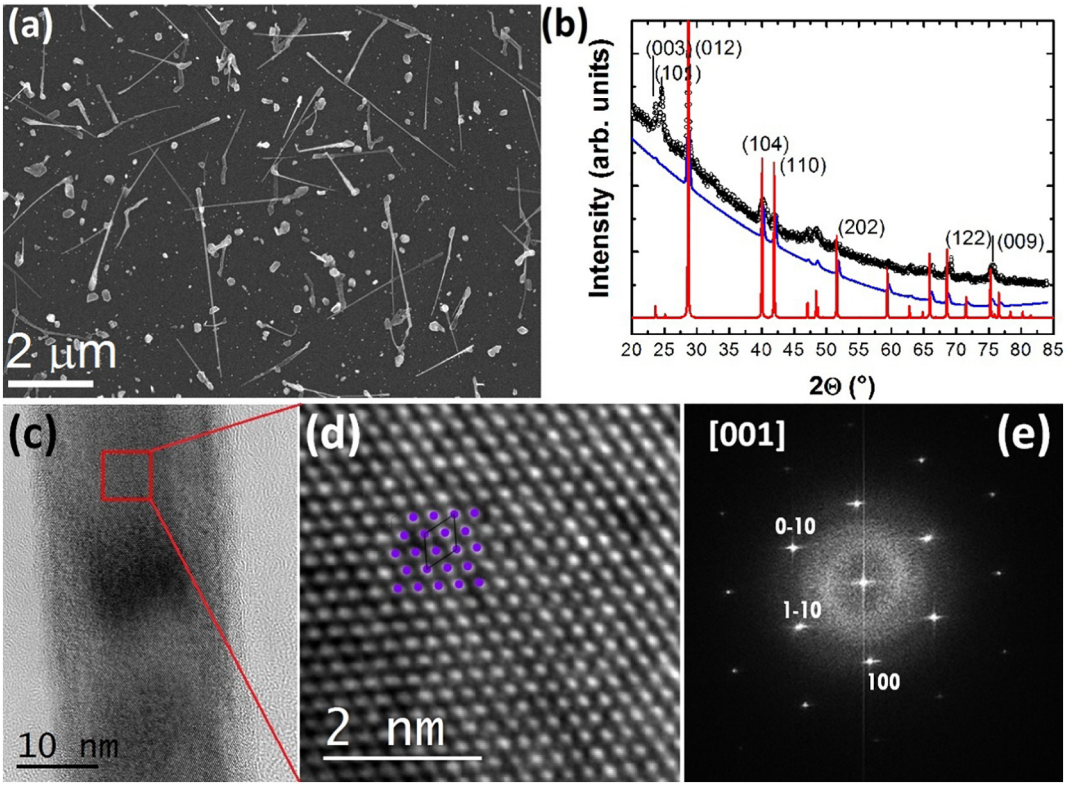

Fig. 1. NWs morphological and structural characterization. (a) SEM top view image of as-grown In-doped Sb NWs. (b) XRD diffraction pattern recorded on the as-grown samples: the data (black circles), the intensity of polycrystalline Sb as from the database [24] (red curve) and the simulated curve (blue line) are shown. HRTEM images at (c) lower and (d) higher magnification of the red square in (c); a ball-and-stick model of the lattice is superimposed for comparison in (d). (e) FFT of the image in (c), indexed as the [001] projection; the main reflections are also labeled.

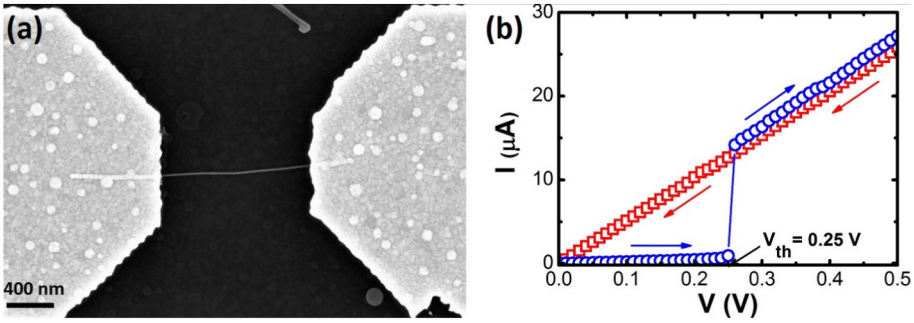

Fig. 2. Electrical measurements. (a) SEM top view image of an In-doped Sb NW, after fabrication of the Ni/Au contacts by EBL, evaporation and lift off. (b) I–V characteristic curve of a device relative to a NW with diameter = 25 nm and distance between the contacts = 650 nm; the high resistance (blue circles and line) and low resistance (red squares) states of the device are reported and the threshold voltage (V_{th}) for the transition from high resistive to low resistive state is indicated. The arrows indicate the direction of the voltage scan.

incorporation of In into the Sb lattice in the NWs shaft. Interestingly, the In–Sb compositions measured by EDX are in the range of values where the crystallization temperature for films of the In–Sb alloy has been reported to be around 150 °C, i.e. close to the one of $Ge_2Sb_2Te_5$ [6,10,11]. Therefore, the thermal stability (i.e. the retention time of the amorphous state) of our In-doped Sb NWs should be comparable to that of $Ge_2Sb_2Te_5$ NWs. A possible reason of the graded content of In in the NW could be linked to a size dependence of the VLS process: the composition of VLS-grown NWs can show a diameter dependence, as observed for instance in Si–Ge NWs [23]. In the present case, and as often observed in VLS growth, a change of diameter is indeed observed during the growth, with the NWs being slightly tapered from bottom to top (Supplementary Information S2). Last, the NW surface was investigated by HRTEM (not shown here) and no oxide layer was detected.

In Fig. 2(a) the SEM image of one harvested NW, after transfer on the measurement substrate and Ni/Au contact fabrication, is displayed. The typical gap between the contacts was (0.5-2.0) μm. Noteworthy, the Te-rich base of the NWs is either cut off during the transfer process or remains buried below the contacts and relatively far from the gapped region. Only the In-doped Sb shaft portion of the NWs was therefore effectively measured in the electrical characterization.

The as-fabricated devices initially showed high resistance values. The reason for this is not clear. Given that the as-grown NWs are crystalline, as shown by the XRD and TEM analysis, the initial high resistance of the devices could be due to the presence of a high contact resistance at the NW-Ni/Au interface. Another possibility is that the as-grown NWs have some defected regions or that such defects are created during the transfer of the NWs from the growth substrates onto the measuring substrates. A few positive and negative I–V scans (for about −3 to +3 V) were performed, during which the resistance of the devices were brought to values of a few tens of ohms. These initial scans could induce the reduction of the contact resistance at the NW-Ni/Au interface or an annealing of the defected regions in the NWs. The devices were then ready for testing their PCM properties.

The memory behavior of the fabricated devices is demonstrated by the presence two distinct states below the threshold voltage (V_{th}): an amorphous (high resistance, reset) and a crystalline (low resistance, set) states. Fig. 2(b) shows the I–V characteristic of a metal-contacted NW device, starting from a reset state of ~ 0.5 MΩ (which was enforced by the application of a 25 ns long, 3 V wide voltage pulse, as it will be explained in the following). As it can be seen in the I–V curve, the device switches to a low resistance state (set state) of 19 kΩ, once the voltage across the NW reaches a threshold (V_{th}) value of ~ 250 mV. On the contrary, the low resistance state shows a linear I–V dependence and is stable at all voltages.

These are all characteristic features of a non-volatile PCM behavior [25]. As for thin film-based devices, the PCM behavior of NWs can be explained in terms of a reversible phase transition of the active material between crystallization and melt-quench amorphization. The set state of our devices clearly shows the linear I–V characteristics expected for the crystalline state of the metallic material. On the other hand, the I–V characteristics of the reset state in the subthreshold regime ($V < V_{th}$) of our NWs are consistent with the existing models for trap-limited conduction in the amorphous state of chalcogenides [26]. In fact, the I–V curves of the NWs in the reset state for $V < V_{th}$ can be fitted by Eq. (1) [26]:

$$I = 2qAN_{T,tot}\frac{\Delta z}{\tau_o}e^{-(E_C-E_F)/kT}\sinh\left(\frac{qV}{kT}\frac{\Delta z}{2u_a}\right) \quad (1)$$

where u_a is the value of the length of the amorphized region of the NW, Δz is the average distance between the traps, q is the elementary charge, E_F is the Fermi level, E_C is the conduction band level, A is the cross section of the NW, $N_{T,tot}$ is the integral of the trap distribution in the gap above the Fermi level, τ_0 is the characteristic attempt-to-escape time for the trapped electron, k is the Boltzmann constant and T is the temperature. The data fitting by Eq. (1) of the measured subthreshold I–V characteristic of an In-doped Sb NW in the reset state is reported in Fig. 3.

As it can be seen in Fig. 3, the I–V curve is well fitted by Eq. (1). From the fit of different NWs in different reset states, the extracted values of u_a vary from 5 to 70 nm (assuming a value of 5 nm for Δz [26]).

The fast switching capabilities of the NWs were proved by performing set and reset operations by extremely short voltage pulses: pulses as short as 25 ns, as measured directly on the device, were sufficient to induce both set and reset (Fig. 4). This pulse duration value ranks among the lowest observed in solid state NW-based PCM devices. In particular, the set pulse duration of the presently investigated NWs is much smaller than that reported for GeTe, $Ge_2Sb_2Te_5$ [27] and $In_3Sb_1Te_2$ [17] NWs. It should also be noticed that 25 ns is the shortest pulse width

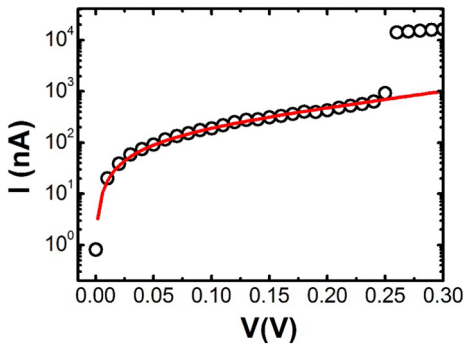

Fig. 3. Fitting by Eq. (1) (red curve) of I–V data (black circles) for $V < V_{th}$, measured on the same NW of Fig. 2(b) in the reset state. The fit provides a value of $u_a = 15$ nm (assuming a value of 5 nm for Δz [26]).

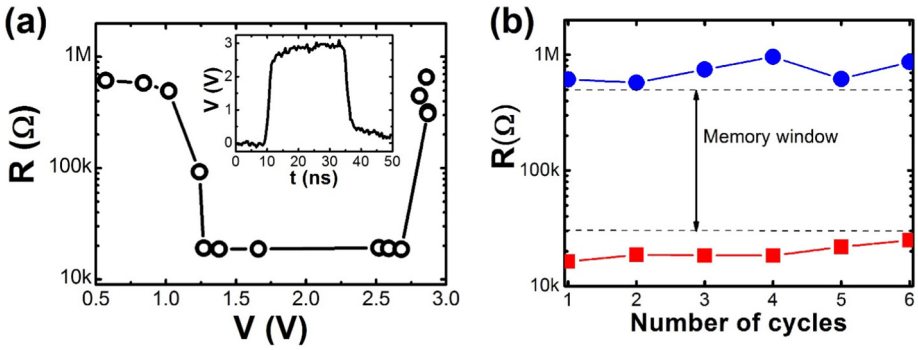

Fig. 4. NWs switching upon application of short voltage pulses. (a) Programing curve: the resistance of a 25 nm thick In-doped Sb NW as a function of the applied voltage pulse amplitude; the pulses duration was 25 ns and their typical shape, measured at the device, is reported in the inset. (b) A mini-cycling test on the same device showing six reversible switches between high (blue circles) and low (red squares) resistance states, obtained with 25 ns voltage pulses of 1.5 and 2.9 V amplitude, for the set and reset operation, respectively. The difference in resistance between the two states is more than one order of magnitude.

we could generate reliably with our system; hence the set and reset processes might be even faster than what we could measure. Also, as the time required for reset is usually smaller than that for set, it is envisaged than the reset time of the presently investigated NWs should indeed be smaller than 25 ns. The voltage amplitude needed for both pulsed set and pulsed reset operations were studied by measuring (at a low enough voltage, 0.02 V, so as not to change the device state) the resistance of the NWs after the application of pulses of increasing voltage amplitude. The resistance of an In-doped Sb NW as a function of the voltage pulse amplitude (i.e. the programing curve) is reported in Fig. 4(a).

The programming curve of Fig. 4(a) shows the typical shape observed in thin film-based $Ge_2Sb_2Te_5$ [25] and NW-based $Ge_2Sb_2Te_5$ [14] and GeTe [28] PCM devices: as the pulse amplitude is increased, the initial high resistance state of the device changes to the low-resistance state for pulses of about 1 V, remains stable for voltages in the range of (1.2–2.7) V and increases to the high-resistance state for larger amplitudes. Based on the programming curve, a mini-cycling test of the same device was performed using voltage pulses of 25 ns duration and of 1.5 and 2.9 V amplitude for the set and reset operation, respectively. In should be stressed here that the studied NWs were not coated by a protective layer during the electrical measurements, which resulted in a limited number of cycles, before the device failed, likely as a consequence of evaporation during the reset operation. One of such cycling tests, reported in Fig. 4(b), clearly shows two distinct memory states, with a resistance gap of more than one order of magnitude, demonstrating the device capability to achieve both set and reset operations with voltage amplitudes typically employed in PCM, while well satisfying the desired performance of high-speed operation. The In-doped Sb NW-based PCM devices also showed promising characteristics in terms of the current and power required for reset, which is typically the most demanding operation in PCM. For the switching cycle test of Fig. 4(b), the average reset current, as converted from the reset voltage and the set state resistance, was ~ 140 μA, corresponding to a reset power of 400 μW and to a reset energy of 10 pJ. These values of reset current and power are larger than those observed in $In_3Sb_1Te_2$ NWs with similar diameters (40 μA and 130 μW for the reset current and power, respectively) [19] and smaller than those reported for 30 nm $Ge_2Sb_2Te_5$ (150 μA, ~ 630 μW) and GeTe (430 μA, ~ 1500 μW) NWs [27]. They are also comparable to the performances of the most advanced PCM devices, where many lithographic steps are required for implementing rather complex architectures (including the realization of crucially important heater and top electrodes) [2,30]. While the integration of bottom-up grown NWs into PCM products remains a technological challenge, these results are yet another confirmation of the beneficial effect of these 1-dimensional nanostructures on the capabilities of PCM devices.

4. Conclusions

In summary, the functional analysis of In-doped Sb NW-based PCM devices gave promising results in terms of power consumption and, in particular, of operational speed, in comparison to the usually employed Ge-Sb-Te alloys for PCM. These findings advance the understanding of Sb-based PCM alloys and of the effects of downscaling to 1-dimensional geometries on the PCM functioning mechanisms. They also contribute to the implementation of innovative nanostructures into the next generation of highly dense and highly performing PCM devices.

Acknowledgements

This work was carried out within the SYNAPSE project, which has received funding from the European Union Seventh Framework Programme (FP7/2007-2013) under grant agreement no. 310339. The authors declare that there is no conflict of interest regarding the publication of this article. The authors would like to acknowledge the Center for Micro- and Nanostructures (ZMNS) at the TU Wien for providing cleanroom facilities.

Appendix A. Supplementary data

Supplementary data to this article can be found online at https://doi.org/10.1016/j.mne.2018.11.002.

References

[1] A. Chen, A review of emerging non-volatile memory (NVM) technologies and applications, Solid State Electron. 125 (2016) 25–38, https://doi.org/10.1016/j.sse.2016.07.006.
[2] S.W. Fong, C.M. Neumann, H.-S.P. Wong, Phase-change memory—towards a storage-class memory, IEEE Trans. Electron Devices 64 (2017) 4374–4385, https://doi.org/10.1109/TED.2017.2746342.
[3] G. Atwood, PCM Applications and an Outlook to the future phase change memory, in: A. Redaelli (Ed.) Springer International Publishing, Cham 2018, pp. 313–324, https://doi.org/10.1007/978-3-319-69053-7.
[4] G.W. Burr, et al., Phase change memory technology, J. Vac. Sci. Technol. B 28 (2010) 223–262, https://doi.org/10.1116/1.3301579.
[5] M. Putero, M.-V. Coulet, T. Ouled-Khachroum, C. Muller, C. Baehtz, S. Raoux, Unusual crystallization behavior in Ga-Sb phase change alloys, APL Mater. 1 (2013) 062101, https://doi.org/10.1063/1.4833035.
[6] E. Suzuki, H. Miura, M. Harigaya, K. Ito, N. Iwata, A. Watada, In-Sb phase-change material for 16× rewritable digital versatile disk, Jpn J. Appl. Phys. 44 (2005) 3598–3600, https://doi.org/10.1116/1.3301579.
[7] J. Solis, C.N. Afonso, Ultrashort-laser-pulse-driven rewritable phase-change optical recording in Sb-based films, Appl. Phys. A Mater. Sci. Process. 76 (2003) 331–338, https://doi.org/10.1007/s00339-002-1817-6.
[8] L. van Pieterson, M. van Schijndel, J.C.N. Rijpers, M. Kaiser, Te-free, Sb-based phase-change materials for high-speed rewritable optical recording, Appl. Phys. Lett. 83 (2003) 1373–1375, https://doi.org/10.1063/1.1604172.

[9] L. van Pieterson, M.H.R. Lankhorst, M. van Schijndel, A.E.T. Kuiper and J.H.J. Roosen, Phase-change recording materials with a growth-dominated crystallization mechanism: Aa materials overview, J. Appl. Phys. 97 (2005), 83250, https://doi.org/10.1063/1.1868860
[10] S.-L. Ou, P.-C. Kuo, S.-C. Sheu, G.-P. Lin, T.-L. Tsai, S.-C. Chen, D.-Y. Chiang, W.-T. Tang, Crystallization mechanisms of $(In_{15}Sb_{85})_{100-x}Bi_x$ phase change recording thin film, Mater. Des. 31 (2010) 1688–1690, https://doi.org/10.1016/j.matdes.2009.01.041.
[11] S.-L. Ou, P.-C. Kuo, S.-C. Sheu, T.-H. Wu, D.-Y. Chiang, W.-T. Tang, Optical properties of nanostructure $(In_{15}Sb_{85})_{100-x}Zn_x$ thin films, Phys. Status Solidi C 4 (2007) 4441–4444, https://doi.org/10.1002/pssc.200777171.
[12] M. Longo, Nanowire phase change memory (PCM) technologies: principles, fabrication and characterization techniques, in: Y. Nishi (Ed.), Advances in Non-Volatile Memory and Storage Technology, Elsevier 2014, pp. 200–230, https://doi.org/10.1533/9780857098092.2.200.
[13] M. Boniardi, A. Redaelli, C. Cupeta, F. Pellizzer, L. Crespi, G. D'Arrigo, A.L. Lacaita, G. Servalli, Optimization metrics for Phase Change Memory (PCM) cell architectures, IEEE International Electron Devices Meeting (IEEE), 2014, https://doi.org/10.1109/IEDM.2014.7047131, p 29.1.1-29.1.4.
[14] S.-H. Lee, Y. Jung, R. Agarwal, Highly scalable non-volatile and ultra-low-power phase-change nanowire memory, Nat. Nanotechnol. 2 (2007) 626–630, https://doi.org/10.1038/nnano.2007.291.
[15] P. Nukala, C.-C. Lin, R. Composto, R. Agarwal, Ultralow-power switching via defect engineering in germanium telluride phase-change memory devices, Nat. Commun. 7 (2016), 10482, https://doi.org/10.1038/ncomms10482.
[16] D. Yu, S. Brittman, J.S. Lee, A.L. Falk, H. Park, Minimum Voltage for Threshold Switching in Nanoscale Phase-Change memory, Nano Lett. 8 (2008) 3429–3433, https://doi.org/10.1021/nl802261s.
[17] J.-K. Ahn, K.-W. Park, H.-J. Jung, S.-G. Yoon, Phase-Change InSbTe Nanowires Grown in Situ at Low Temperature by Metal−Organic Chemical Vapor Deposition, Nano Lett. 10 (2010) 472–477, https://doi.org/10.1021/nl903188z.
[18] S. Selmo, S. Cecchi, R. Cecchini, C. Wiemer, M. Fanciulli, E. Rotunno, L. Lazzarini, M. Longo, MOCVD growth and structural characterization of In-Sb-Te nanowires, Phys. Status Solidi A 213 (2016) 335–338, https://doi.org/10.1002/pssa.201532381.
[19] S. Selmo, et al., Low power phase change memory switching of ultra-thin $In_3Sb_1Te_2$ nanowires, Appl. Phys. Lett. 109 (2016), 213103, https://doi.org/10.1063/1.4968510.
[20] H. Hardtdegen, M. Hollfelder, R. Meyer, R. Carius, H. Münder, S. Frohnhoff, D. Szynka, H. Lüth, MOVPE growth of GaAs using a N_2 carrier, J. Cryst. Growth 124 (1992) 420–426, https://doi.org/10.1016/0022-0248(92)90494-4.
[21] M. Sauter, W. Simbürger, D. Johnsson, M. Stecher, On-wafer measurement of the reverse-recovery time of integrated diodes by Transmission-Line-Pulsing (TLP), Microelectron. Reliab. 51 (2011) 1309–1314, https://doi.org/10.1016/j.microrel.2011.02.012.
[22] C.S. Barrett, P. Cucka, K. Haefner, The crystal structure of antimony at 4.2, 78 and 298° K, Acta Crystallogr. 16 (1963) 451–453, https://doi.org/10.1107/S0365110X63001262.
[23] X. Zhang, K.-K. Lew, P. Nimmatoori, J.M. Redwing, E.C. Dickey, Diameter-Dependent Composition of Vapor-Liquid-Solid Grown $Si_{1-x}Ge_x$ Nanowires, Nano Lett. 7 (2007) 3241–3245, https://doi.org/10.1021/nl071132u.
[24] File n° 9859, in: FitzKarsruhe, Inorganic crystal structure database, 2017.
[25] A. Pirovano, et al., μTrench phase-change memory cell engineering and optimization, Proceedings of 35th European Solid-State Device Research Conference, 2005. ESSDERC 2005, IEEE 2005, pp. 313–316, https://doi.org/10.1109/ESSDER.2005.1546648.
[26] D. Ielmini, Y. Zhang, Analytical model for subthreshold conduction and threshold switching in chalcogenide-based memory devices, J. Appl. Phys. 102 (2007), 54517, https://doi.org/10.1063/1.2773688.
[27] S.-H. Lee, Y. Jung, H.S. Chung, A.T. Jennings, R. Agarwal, Comparative study of memory-switching phenomena in phase change GeTe and $Ge_2Sb_2Te_5$ nanowire devices, Phys. E Low-Dimensional Syst. Nanostructures 40 (2008) 2474–2480, https://doi.org/10.1016/j.physe.2007.09.171.
[28] S.-H. Lee, D.-K. Ko, Y. Jung, R. Agarwal, Size-dependent phase transition memory switching behavior and low writing currents in GeTe nanowires, Appl. Phys. Lett. 89 (2006), 223116, https://doi.org/10.1063/1.2397558.
[29] F. Pellizzer, in: A. Redaelli (Ed.), Phase-Change Memory Devices Architecture Phase Change Memory, Springer International Publishing, Cham 2018, pp. 263–284, https://doi.org/10.1007/978-3-319-69053-7.